Nanoscale

PAPER

Cite this: *Nanoscale*, 2022, **14**, 3078

Efficient mechanical modulation of the phonon thermal conductivity of Mo_6S_6 nanowires†

Ke Xu,‡[a] Shichen Deng,‡[b] Ting Liang,[c] Xuezheng Cao,[a] Meng Han,[c] Xiaoliang Zeng,[c] Zhisen Zhang,[a] Nuo Yang *[b] and Jianyang Wu *[a,d]

Received 29th December 2021,
Accepted 25th January 2022

DOI: 10.1039/d1nr08505k

rsc.li/nanoscale

Mo_6S_6 nanowires are emerging as key building blocks for flexible devices and are competitive with carbon nanotubes due to easier separation and functionalization. Here, it is reported the phonon thermal conductivity (κ) of Mo_6S_6 nanowires *via* molecular dynamics simulations. It shows a large tunability of low-frequency phonon thermal conductivity $(\kappa_{lf})^{A}_{max}$ from 27.2–191 W (m K)$^{-1}$, an increase of around 702% *via* mechanical strain. Below critical tension/torsion strain, their phonon thermal conductivity monotonically reduces/enlarges; whereas above this value, an inverse trend is identified. On the other hand, Mo_6S_6 nanowires show unusual auxetic behavior. The transitions involved in phonon thermal conductivity are molecularly illustrated by a strain-induced crossover in bond configurations and are explained based on a competition mechanism between phonon scattering and group velocity. This study provides insights into the thermal transport and auxetic properties of low-dimensional structures and the thermal management of Mo_6S_6 nanowire-based systems.

1 Introduction

Chalcogenides of molybdenum are able to form intriguing stable two- and one-dimensional (2D and 1D) structures with unique chemical, electronic and mechanical properties that are not identified in their three-dimensional (3D) bulk counterparts.[1–5] Monolayered molybdenum disulfide (MoS_2) and MoS_2 nanotubes (NTs) are nanomaterials representative of 2D and 1D molybdenum chalcogenide structures, respectively. The 1D hollow fullerene-like MoS_2 NTs, similar to carbon nanotubes (CNTs),[6,7] are structurally constructed by the wrapping of MoS_2 monolayer sheets.[8]

Recently, a new 1D Mo_6S_6 nanowire (NW), which was physically achievable from MoS_2 sheets, has been experimentally produced in bulk quantities from van der Waals (vdW) bonded bundles of parallel NWs in lab settings,[3,9,10] in sharp contrast to CNTs. To date, there have been pioneering investigations revealing the unique electronic, transport and mechanical properties as well as the well-defined structural behaviors of Mo_6S_6 NWs.[3,11–15] For example, it was revealed from both experimental and theoretical studies that Mo_6S_6 NWs show uniaxial metallic characteristics[3,9,11,16] resulting from the strong hybridization between the Mo d-orbitals and S p-orbitals.[10] Furthermore, the structural behaviors and the electronic and transport properties of Mo_6S_6 NWs are tunable by twisting and/or defect engineering rather than bending strain engineering. Intriguingly, a metal-to-semiconductor transition is induced as the NW is critically twisted.[11,16,17] The mechanical stiffness of the Mo_6S_6 NW is represented by its elastic modulus of around 320 GPa,[18] which makes it more mechanically robust than NWs of other transition metal dichalcogenides, including Mo_6Se_6 and Mo_6Te_6 NWs as well as steel.[16,19,20]

As a result of its unique properties and easy availability, isolated Mo_6S_6 NWs are emerging as important building blocks for the fabrication of robust flexible nanoscale electronics, and are competitive with CNTs. However, it is well-known that the issues of efficient heat dissipation and the thermal management of flexible electronic devices remain unresolved.[21,22] Thus, a fundamental understanding of thermal transport behavior in isolated Mo_6S_6 NWs is highly desirable in order to advance their practical applications in making flexible nanodevices with, for example, improved performance and extended lifetime. To date, unlike CNTs,[23–25] the thermal

[a]*Department of Physics, Research Institute for Biomimetics and Soft Matter, Jiujiang Research Institute and Fujian Provincial Key Laboratory for Soft Functional Materials Research, Xiamen University, Xiamen 361005, PR China. E-mail: nuo@hust.edu.cn*
[b]*State Key Laboratory of Coal Combustion, and School of Energy and Power Engineering, Huazhong University of Science and Technology (HUST), Wuhan, 430074 PR China. E-mail: jianyang@xmu.edu.cn*
[c]*Shenzhen Institute of Advanced Electronic Materials, Shenzhen Institutes of Advanced Technology, Chinese Academy of Sciences, Shenzhen 518055, PR China*
[d]*NTNU Nanomechanical Lab, Norwegian University of Science and Technology (NTNU), Trondheim 7491, Norway*

†Electronic supplementary information (ESI) available. See DOI: 10.1039/d1nr08505k

‡These authors contributed equally to this work.

transport characteristics of Mo_6S_6 NWs are still unknown, let alone the thermal responses to deformation that inevitably occur when used as components of nanodevice systems.

This work reports the phonon thermal conductivity (κ), and low-frequency phonon thermal conductivity $(\kappa_{lf})^A_{max}$ of mechanically-deformed Mo_6S_6 NW *via* non-equilibrium molecular dynamic (NEMD) simulations. Crossover was identified in phonon thermal conductivity as well as the low-frequency phonon thermal conductivity and Poisson's ratio of Mo_6S_6 NWs as it is critically axially elongated, leading to an axial strain-induced transition in the auxetic property. Then, the crossover in its phonon thermal conductivity could be critically attributed to the competition mechanism between phonon scattering and group velocity. Finally, it is explained that transitions of the low-frequency phonon thermal conductivity and Poisson's ratio originate from its unique molecular structure.

2 Models and methods

Fig. 1a–f present the atomic structure of the Mo_6S_6 NW with finite axial length when viewed from different angles, and the Mo and S atoms are blue- and yellow-colored, respectively. As shown in Fig. 1a, c and d, one crystalline unit cell of a free-standing Mo_6S_6 NW is structurally dominated by a backbone skeleton composed of Mo_6 octahedra that are dressed with six sulfur (S) anions each on the surface.[10] From the molecular point of view, as shown in Fig. 1b, the unit cell of the NW is composed of two staggered atomic triangles, each of them containing three Mo and three S atoms. Within each triangle, the S-atoms are located at the corners, and one Mo atom is situated between each S pair. The six Mo atoms in the staggered atomic triangles structurally form an octahedron. Fig. 1c and d show two side-view snapshots of a non-strained Mo_6S_6 NW, while Fig. 1e and f display the perspective snapshots of the twist-free and twisted Mo_6S_6 NWs with finite axial length, respectively (see Fig. S1† for the detailed structure under torsional strain).

All MD simulations were implemented using the open-source code Large-scale Atomic/Molecular Massively Parallel Simulator (LAMMPS) package[26,27] with ReaxFF forcefield. ReaxFF is a popular forcefield used to predict the properties of a variety of material systems.[28–31] For the Mo_6S_6 NW system, the version of ReaxFF potential developed by Ostadhossein *et al.* was employed for describing the atomic interactions.[32] This version of ReaxFF potential has been successfully applied to predict the thermal properties of MoS_2-based and molybdenum sulfide nanostructures.[32–34] On the other hand, the widely used forcefields Mo–S type REBO[35] and SW[36] were tested, whereas they were not able to structurally stabilize the Mo_6S_6 NW at a finite temperature of 300 K, let alone predict the thermal conductivity. Moreover, a small timestep of 0.2 fs was adopted to ensure energy conservation within the ReaxFF forcefield in the NEMD simulations. By directly collecting the heat flow of the heat source and the heat sink, the statistical errors related to heat flow in the MD calculations with multi-body potential were eliminated. A Mo_6S_6 NW with approximately 230 nm axial length was constructed by replicating its unit cell. Then, the relaxed Mo_6S_6 NW was mechanically deformed to examine the strain effect on thermal conduction.

To achieve the deformed Mo_6S_6 NW, the relaxed Mo_6S_6 NW was uniformly elongated/twisted over the wire axial length at different strains. The NEMD approach was adopted to calculate the phonon thermal conductivity of the non-strained and strained Mo_6S_6 NWs, as shown in Table S2 and Fig. S2.† To introduce a stable heat flow along the axial direction, the heat source and heat sink are imposed at the ends of the Mo_6S_6 NW. Then, a temperature gradient ΔT was established by generating a nonequilibrium heat flux Q, and κ was calculated according to the Fourier law, as follows:

$$\kappa = \frac{Q}{|\Delta T|} \tag{1}$$

where Q is generated by coupling the source region of the system with a high temperature of 315 K and the sink region at a low temperature of 285 K to a thermostat, with the tempera-

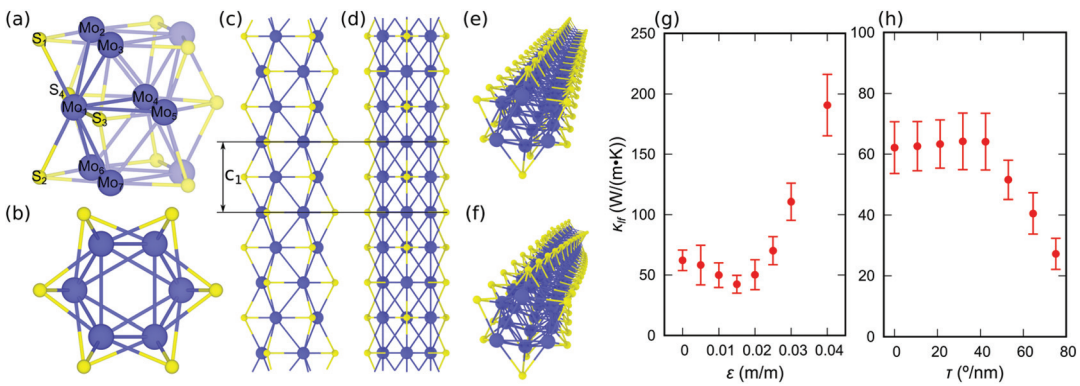

Fig. 1 Atomic structure and low-frequency phonon thermal conductivity (κ_{lf}) of an isolated Mo_6S_6 nanowire. (a)–(e) Atomic models of a deformation-free isolated Mo_6S_6 nanowire. (f) Perspective of a representative twisted Mo_6S_6 nanowire, in which the specific torsional strain (τ) equals 11.5° nm^{-1}. For clarification, Mo and S atoms are rendered in blue and yellow, respectively. (g) and (h) Variation in the κ_{lf} of the Mo_6S_6 nanowire with tensile and torsional strain, respectively.

tures of both regions controlled by the Nosé–Hoover chain method. The heat flux Q was calculated from the energy transfer rate dE/dt between the source/sink region and the thermostat:

$$Q = \frac{dE/dt}{S} \tag{2}$$

where S is the cross-sectional area perpendicular to the transport direction. Here, the diameter of the Mo_6S_6 NW was chosen as 0.6 nm.[37]

The spectral thermal conductivity in this paper was solved by setting an imaginary cross-section. The spectral heat current between the atoms i and j at both ends of the imaginary cross-section can be expressed as:[15]

$$q_{i\to j}(\omega) \approx -\frac{2}{t_{\text{simu}}\omega}\sum_{\alpha,\beta\in\{x,y,z\}} \text{Im}\left\langle \hat{v}_i^{\alpha}(\omega)\cdot K_{ij}^{\alpha\beta}\hat{v}_j^{\beta}(\omega)\right\rangle$$

where t_{simu} and ω are the simulation time and frequency, respectively. The velocities $\hat{v}_i^{\alpha}(\omega)$ and $\hat{v}_j^{\beta}(\omega)$ are the Fourier transform of the atomic velocity of atom i in the α direction and that of atom j in the β direction, respectively. $K_{ij}^{\alpha\beta}$ is the force constant matrix. The heat current across any interface separating disjoint atom sets (Gl and Gr) was obtained by summing over atoms in each set:

$$q(\omega) = \sum_{i\in\text{Gl}}\sum_{j\in\text{Gr}} q_{i\to j}(\omega)$$

Furthermore, the spectral decomposition thermal conductivity was calculated as follows:

$$\kappa(\omega) = \frac{q(\omega)}{A\Delta T}$$

By using the spectral decomposition thermal conductivity, the thermal conductivity in any frequency region can be determined. Generally, the thermal conductivity of low-dimensional materials is mainly contributed by the acoustic branch of the phonon.[38] As a result, the thermal conductivity of the Mo_6S_6 NW in the low-phonon-frequency region is primarily discussed in this study.

The tensile strain and torsional strain are defined as $\varepsilon = (L - L_0)/L_0$ and $\tau = d\theta/dL$, respectively, where L_0 and L are the axial lengths of the original and deformed nanowires, respectively, and θ is the torsion angle. Poisson's ratio (μ) is defined by the negative of the ratio of the contraction strain (transverse, lateral or radial strain, ε_t) to the loading strain (or axial strain, ε_l), expressed by the formula $\mu = -\varepsilon_t/\varepsilon_l$.

The vibrational density of state (νDOS), $g(\omega)$, was calculated from the Fourier transform of the atomic velocity auto-correlation functions (VACFs) $G(t)$, which is expressed as:

$$\begin{aligned} G(t) &= \langle v_i(\tau)\cdot v_i(\tau+t)\rangle_{i,\tau} \\ &= \frac{1}{N}\sum_{i=1}^{N}\frac{1}{t_{\text{int}}-t}\int_0^{t_{\text{int}}-t} v_i(\tau)\cdot v_i(\tau+t)d\tau \end{aligned} \tag{3}$$

where t_{int} is the time of integration, N is the total number of atoms in the ensemble, v_i is the velocity vector of the ith atom, and $\langle\rangle$ stands for the ensemble average. Based on the VACFs, $g(\omega)$ can be computed as:

$$\begin{aligned} g(\omega) &= \int_0^{t_{\text{int}}} G(t)^{-i\omega t}dt \\ &= \int_0^{t_{\text{int}}} \langle v_i(\tau)\cdot v_i(\tau+t)\rangle_{i,\tau} e^{-i\omega t}dt \end{aligned} \tag{4}$$

The SED function $\Phi(k,\omega)$ is expressed as:

$$\begin{aligned} \Phi(k,\omega) = \frac{1}{4\pi t_{\text{int}}N_{\text{T}}}\sum_{\alpha}\sum_{b}^{B} m_b\Big|\int_0^{t_{\text{int}}}\sum_{n_i}^{N_{\text{T}}} v_\alpha(n_i,b,t) \\ \times \exp[ik\cdot r(n_i) - i\omega t]dt\Big|^2 \end{aligned} \tag{5}$$

where N_{T} is the total number of unit cells, B is the number of atoms per unit cell (B = 12 for the unit cell chosen for tensile strain system), and $v_\alpha(n_i,b,t)$ is the velocity of atom b (with mass m_b) inside the unit cell n_i in the α direction.

3 Results and discussion

As shown in Fig. S3a,† it is found that the phonon spectrogram of the Mo_6S_6 NW in the acoustic branch phonon region predicted by ReaxFF-based MD calculations is in good agreement with that obtained by density functional theory (DFT) calculations. Moreover, the κ_{lf} of the Mo_6S_6 NW subjected to zero strain was largely contributed by the low-frequency region. Such a case was also observed when the Mo_6S_6 NW was stretched and twisted, as shown in Fig. S3b and c.† Therefore, the dependence of κ_{lf} on mechanical strain is mainly dictated by the low-frequency contributions. Besides, the low frequency means the frequency (ω) is smaller than max value of the acoustic branch (ω^A_{max}), where $\omega^A_{\text{max}} \approx 10$ THz, and $\omega^A_{\text{max}} \approx 20$ THz when $\varepsilon \geq 0.03$. The value of κ_{lf} of the Mo_6S_6 NW was calculated from the spectral decomposition thermal conductivity, as shown in Fig. S3b and c.† There is a minor contribution from the low-frequency optical branch to the κ_{lf}. Besides, the optical branches predicted by ReaxFF has a large difference from the DFT. Gennerally, the contribution from the high-frequency optical branch phonons to the thermal conductivity could be neglected, due to its low group velocity. As such, the κ_{lf} of the Mo_6S_6 NW is discussed in this work if not specified otherwise, while the values of κ (at all frequencies) is shown in Fig. S4.† Therefore, the κ_{lf} of the Mo_6S_6 NW calculated by the ReaxFF-based MD calculations is reliable. More information can be found in section 3.2 of ESI.†

The main results of κ_{lf} are shown in Fig. 1g and h, which show the variations in the κ_{lf} of the Mo_6S_6 NW with axial tension strain and specific torsional angle, respectively. In addition, the κ of the Mo_6S_6 NW with axial tension strain and specific torsional angle is displayed in Fig. S4.† Obviously, the κ_{lf} of the Mo_6S_6 NW was finely tuned by both axial tension strain and torsional strain. At zero strain, the Mo_6S_6 NW showed a κ_{lf} of around 62.2 W (m K)$^{-1}$, which is higher/lower than those of its low-dimensional counterparts MoS_2 NTs[39]/MoS_2 monolayers, respectively.[40] Under axial elongation, the

Mo_6S_6 NW showed a clear reduction in κ_{lf} by around 32% as the axial tension strain varied from 0–0.015. Such tension-strain-driven degradation in κ_{lf} has been also identified in low-dimensional structures, such as MoS_2 NTs[39] and MoS_2 monolayer sheets,[41,42] graphene and CNTs.[43] When the axial tension strain is over 0.015, however, the Mo_6S_6 NW inversely exhibits an improvement in κ by about 451% at an axial tension strain of 0.04, which is greater than the modulation of thermal conductivity achieved by the pinching effect,[44,45] folding effect,[46,47] resonance hybridization effect,[48–51] light-responsive[52] and electric field.[53,54] This phenomenon of monotonic enhancement in κ_{lf} caused by the tensile strain also occurs in 1D black phosphorus NT[55] and 2D single-layer phosphorene.[56] More notably, such tension-strain-induced crossover in the κ_{lf} of the Mo_6S_6 NW has not been reported in other 1D structures.

When subjected to twisting, an inverse crossover in the κ_{lf} of the Mo_6S_6 NW was intriguingly identified, as shown in Fig. 1h. When the specific torsional angle was enlarged from 0 to 42.4° nm^{-1}, the κ_{lf} of the Mo_6S_6 NW monotonically increased by around 3.3%. Such twist-induced monotonic enhancement in κ_{lf} has been reported in multi-chain graphene NT,[43] polyethylene[57] and graphene nanoribbons.[58,59] Once the specific torsional angle exceeded 42.4° nm^{-1}, however, there was a pronounced reduction in κ by 58% at a specific torsional angle of around 75.2° nm^{-1}. In a nutshell, in comparison with other 1D materials,[39,57,60–62] Mo_6S_6 NW showed more effective tunability and crossover of κ_{lf} *via* tension/torsional strain engineering.

On the other hand, it is well known that the size effect influences the κ (at all frequencies) of low-dimensional materials. As a result, the size effect on the κ of the Mo_6S_6 NW is also examined. Fig. S5a† shows the variation in the κ of the Mo_6S_6 NW with axial length. It revealed that the thermal conductivity of the Mo_6S_6 NW followed $\kappa \propto L^{\beta}$ and here $\beta = 0.31$. This suggests that the κ of the Mo_6S_6 NW follows the one-dimensional (1D) nonlinear lattice model. The results are in good agreement with the previous prediction on 1D nanostructures that the κ of 1D materials is length-dependent.[63,64] In this study, Mo_6S_6 NWs with a fixed finite axial length of 230 nm were generated to reveal the role of the tension and torsion strains on κ and κ_{lf}. More information can be found in section 2.4 of ESI.†

In one-dimensional materials, phonon transport is largely limited by boundary scattering due to the classical size effect,[48,65] but it can be significantly enhanced by the hydrodynamic phonon flow when the normal (N) process was much larger than the Umklapp (U) process.[66] As a result, the three-phonon scattering rates of the Mo_6S_6 nanowire subjected to zero strain were calculated, as shown in Fig. S5b.† As indicated, the normal process was found to be around 2 orders of magnitude stronger than the Umklapp process in the low-frequency range (<1 THz), thereby explaining that the extremely high κ_{lf} of the Mo_6S_6 nanowire might partially be caused by the hydrodynamic effects.[66,67]

To provide physical insights into the deformation-induced crossover in κ_{lf}, the vibrational density of states (νDOS) of the molecular structures in the wire-axial direction were calculated. Fig. 2a and b plot the νDOS ($\omega < \omega^{A}_{max}$) spectra of the Mo_6S_6 NW subjected to different axial tensile strains and specific torsional angles, respectively, while the full-frequency νDOS spectra of the Mo_6S_6 NW is shown in Fig. S4b.† As shown in Fig. 2a, when axial tension strain is increased from 0 to 0.015, insignificant changes were identified in the low-frequency phonon modes. The frequencies of the phonon modes were red-shifted,[59,68] but there was no noticeable change in the shape of the νDOS spectra, indicative of a decrease in the

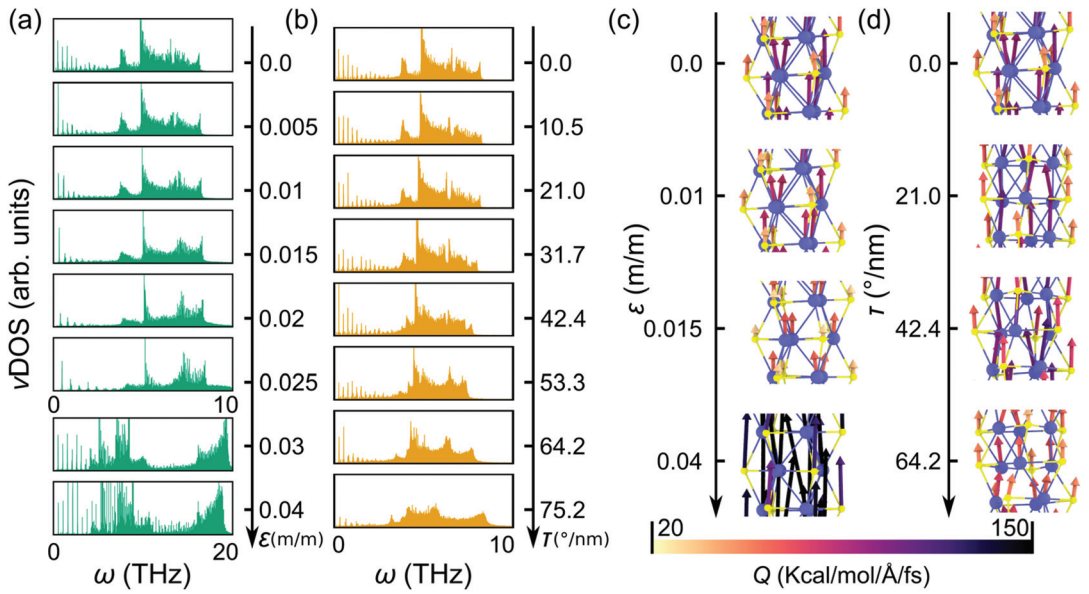

Fig. 2 (a) and (b) Vibrational density of states in isolated Mo_6S_6 nanowires subjected to different tensile (ε) and torsional (τ) strains, respectively, at a frequency $\omega < \omega^{A}_{max}$. (c) and (d) Vectors of atomic heat flux in Mo_6S_6 nanowires subjected to four different tensile and torsional strains.

velocity of the phonon group. On the basis of $\kappa = Cv^2\tau/3$, a decrease in the velocity of the phonon group causes a reduction in κ. When the axial tension strain was above 0.015, dramatic changes were observed in the distribution and shape of the νDOS spectra.

During twisting deformation, when the specific torsional angle was less than 42.4° nm^{-1}, there was no remarkable change in the shape of the νDOS spectra, explaining the insignificant change in the κ_{lf} of the Mo_6S_6 NW subjected to small torsional strains. When the specific torsional angle applied was over 42.4° nm^{-1}, however, the phonon modes shifted to a lower frequency region, resulting in a decrease in the velocity of the phonon group. In addition, it was found that a number of sharp peaks of νDOS were flattened or even disappeared under large torsional strain, for example, under twisting at 75.2° nm^{-1}, leading to increased phonon scattering. It can be summarized that a combination of those two aspects causes the reduction in the κ_{lf} of the Mo_6S_6 NW under torsional strains over 42.4° nm^{-1}.

Moreover, on examining the microscopic heat flux diagrams of the Mo_6S_6 NW, as shown in Fig. 2c and d, it was evident that there were significant differences in the contributions of distinct atoms to heat flow along the NW at different strains. Apparently, much more axial heat flux was carried through the Mo atoms, which are the skeleton of NW, than through the surface S atoms. This clearly indicates the greater contribution of Mo atoms to the global axial κ_{lf} than the S atoms.

To reveal the effect of strain on the phonon properties in detail, the spectral energy density (SED) of the Mo_6S_6 NW is computed under different strains, which has been widely used to understand the thermal properties of low-dimensional materials.[69–71] Fig. 3a shows the SED spectrum ($\omega < \omega^A_{max}$) of the Mo_6S_6 NWs at critical axial tension strains of 0, 0.015 and 0.04, while the full-frequency SED spectrum is shown in Fig. S6.† The blue dashed lines are the acoustic phonon dispersion relation curves of the Mo_6S_6 NW at zero strain obtained from the DFT calculations. It could be observed that the blue dashed lines were in good agreement with the SED curves based on the MD calculations, confirming the reliability of the SED results. As the axial tension strain was increased from 0 to 0.015, the shape of the dispersion curves slightly changed, with the phonon branches moving towards the lower-frequency region, resulting in a slight decrease in the velocity of the phonon group ($\omega < \omega^A_{max}$), as shown in Fig. 3c. Moreover, an apparent broadening in the dispersion curves was observed with increasing axial tension strain, indicating the enhancement of phonon scattering and shortening of the phonon lifetime. Tension-induced changes in phonon properties have also been identified in other low-dimensional materials, such as penta-SiN_2.[72] This clearly explains the reduction of κ_{lf} with the axial tension strain increasing from 0 to 0.015. When the axial tension strain was increased to 0.04, however, dramatic changes in the SED curves could be observed. Moreover, the low-frequency phonon branches, particularly the LA branch, became much steeper, thereby resulting in higher phonon group velocities in the Mo_6S_6 NW under the axial tension strain of 0.04 than that at zero strain, as shown in Fig. 3c. The phenomenon of strain-induced increase in the acoustic frequency has also been reported in black phosphorus[55,73] and monolayer silicene.[59] This explains the high κ_{lf} of the Mo_6S_6 NW under large axial tension strains. As revealed, the axial-tension-strain-induced crossover in κ_{lf} can be attributed to the changes in two factors, namely phonon scattering and phonon group velocity. Phonon scattering becomes pronounced with increasing axial tension strain. The phonon group velocities decrease under small tensile strains, thereby suppressing heat transport. However, under large tensile strains, a dramatic increase in group velocities significantly promotes heat transport, which wipes away the influence of phonon scattering.

Fig. 3b shows the SED spectrum ($\omega < \omega^A_{max}$) of the Mo_6S_6 NW under the critical specific torsional angles of 21.0, 42.4 and 64.2° nm^{-1}. The dense dispersion curves are due to the long periodic length and more atoms in the minimum repetition unit of the Mo_6S_6 NW considered for achieving uniform twisting deformations. As the specific torsional angle was enlarged from 21.0 to 42.4° nm^{-1}, there were relatively small differences in the dispersion curves, and the calculated phonon group velocities of the acoustic phonons were slightly higher under 42.4° nm^{-1}. This explains the relatively slight increase in the κ_{lf} of the Mo_6S_6 NW under small torsional deformations. As the specific torsional angle is increased to 64.2° nm^{-1}, however, an obvious decrease in the phonon group velocities can be observed, as shown in Fig. 3d, as well as a broadening effect (Fig. S6†), which corresponds to the changing trend of νDOS seen in Fig. 4. Therefore, a combination of the increase in phonon scattering and a decrease in phonon group velocities are responsible for the reduction in

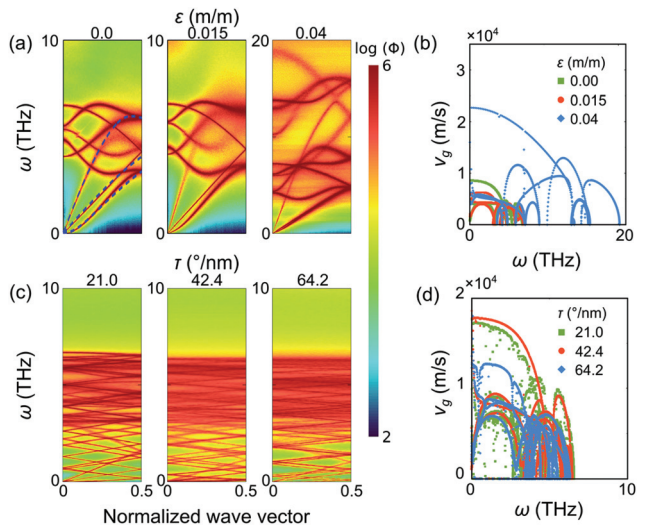

Fig. 3 (a) and (c) Phonon dispersion relationship in isolated Mo_6S_6 nanowires subjected to three different critical tensile (ε) and torsional (τ) strains, respectively. (b) and (d) Phonon group velocity as a function of frequency in isolated Mo_6S_6 nanowires under three critical tensile and torsional strains, respectively. $\omega < \omega^A_{max}$.

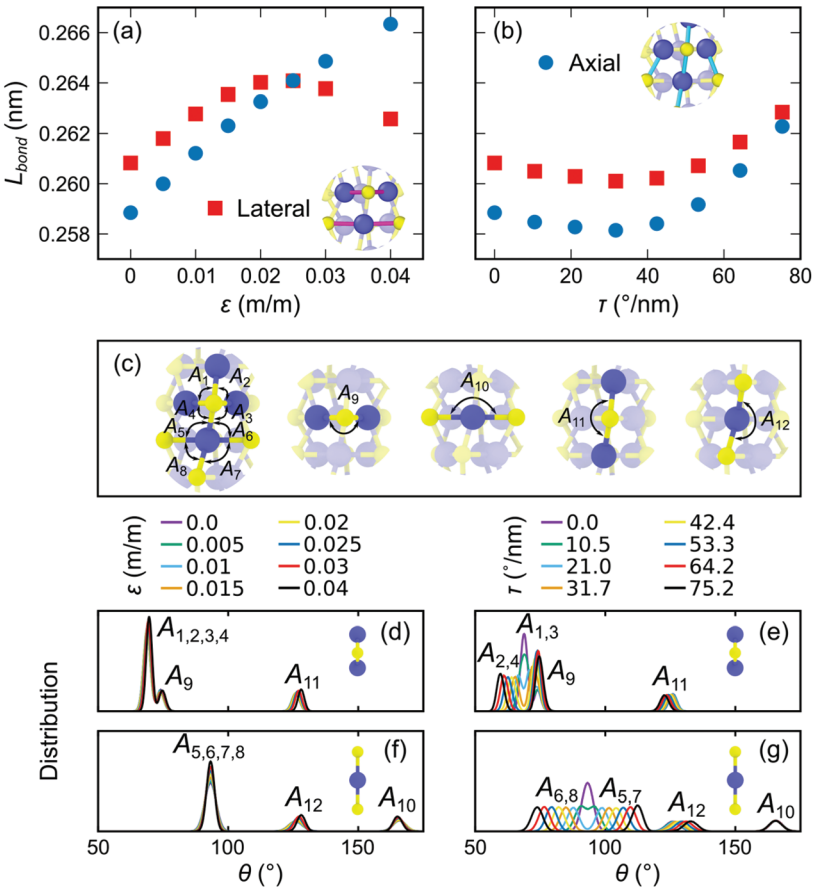

Fig. 4 Characteristics of bond configuration in mechanically deformed Mo_6S_6 nanowires. (a) and (b) Average bond length (L_{bond}) of Mo–S as a function of tensile (ε) and torsional (τ) strain, respectively. Here, two critical oriented Mo–S bonds that make angles of 0° and 90° with the wire axial direction are considered for the investigation of bond lengths, termed as axial and lateral, respectively. (c) Schematic diagrams of the 12 distinct bond angles in the Mo_6S_6 nanowires. Distribution profiles of Mo–S–Mo (d and f) and S–Mo–S (e and g) bond angles at different tensile (ε) and torsional (τ) strains, respectively.

the κ_{lf} of the Mo_6S_6 NW subjected to large torsional deformations.

Such intriguing transitions in the κ_{lf} of the Mo_6S_6 NW could be molecularly explained based on the deformation-induced changes in its bond configurations, such as bond distances and bond angles. Fig. 4a and b show the average bond distances of the two critically oriented Mo–S bonds that make an angle of either 0° or 90° to the axial direction of the Mo_6S_6 NW as a function of the axial tension and torsional strain, respectively. The distribution of the bond distances is presented in Fig. S7.† During axial elongation, the two oriented Mo–S bonds present distinct changes in their average bond distances. The Mo–S bonds that make 0° to the wire axial direction were monotonically elongated with increasing axial tension strain, and the bond elongation became more pronounced with the augmentation of axial tension strain. However, there is a crossover in the bond distance of the Mo–S bonds at 90° to the wire axial direction at an axial tension strain of 0.025, below which these Mo–S bonds are monotonically stretched, and bond stretching becomes less pronounced with increasing axial tension strain. However, above this value, they are monotonically compressed and bond compression becomes more pronounced with increase in axial tension strain. It must be noted that, remarkably, the elongation of the Mo–S bonds with the orientation angle of 90° to the wire axial direction suggests auxetic behavior in the lateral cross-section of the Mo_6S_6 NW.

Under uniform twisting operation, there were also significant changes in the bond distances of both the critically oriented Mo–S bonds. Interestingly, both oriented Mo–S bonds showed similar crossovers for the change in bond distances at the critical specific torsional angle of around 42.4° nm^{-1}. At angles below this, both oriented Mo–S bonds are monotonically contracted and the bond contraction becomes less pronounced with increasing torsional strain, whereas at higher angles, they are elongated and bond elongation is more pronounced with the augmentation of torsional strain. Remarkably, this "flipped" behavior in the change of bond distance differs from that of the NW subjected to axial tension. Fig. 4c–g present the structural information of the bond angles in the Mo_6S_6 NWs at different deformation levels. There were around six distinct bond angles in the Mo_6S_6 NW at zero

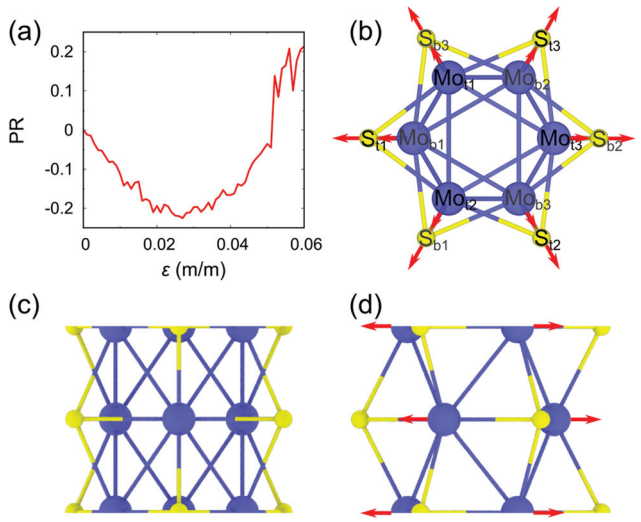

Fig. 5 Schematic diagram of the atom movement trend in the Mo_6S_6 nanowire under small tensile strain (ε). (a) The change in Poisson's ratio (PR) during tensile strain. (b), (c) and (d) are the top view, side view and front view, respectively. The red arrow indicates the movement trend of atoms: (b) Mo and S atoms; (d) Mo atoms.

strain, including 68.5°, 74.0°, 93.0°, 125°, 126° and 165°. Under axial straining, the Mo_6S_6 NW shows small changes in these bond angles, whereas, under twisting, it shows notable bond angle changes. From the molecular structure point of view, the unique transitional changes in the bond configurations of the 1D Mo_6S_6 NW are the main source of the crossovers in its κ_{lf} and Poisson's ratio trends. In addition, this strain-induced crossover in the κ_{lf} values is very different from the cases of other materials, such as amorphous silicon dioxide thin films,[74] bulk epoxy resins,[75] polymers[76] and monolayer silicene,[77] borophene,[78] 2D penta-structures,[72] and single-layer phosphorene.[79]

To quantitatively show the auxetic property of the Mo_6S_6 NW, its Poisson ratio was calculated. As shown in Fig. 5a, the Mo_6S_6 NW yielded an apparent negative Poisson's ratio with a minimum value of around −0.2 and presented a transition in Poisson's ratio at a strain of around 0.026 as a result of its unique structural motif. As illustrated in the top and front views of the Mo_6S_6 NW in Fig. 5b and d, respectively, both inner Mo and outer S atoms showed displacement vectors toward the outside of the nanowire when it was axially stretched, resulting in a negative Poisson's ratio. To date, negative Poisson's ratios have been reported for 2D materials[80–87] as well as artificially designed nanostructures;[87–91] however, 1D materials with negative Poisson's ratios have rarely been observed.

4 Conclusions

In summary, the critical role of mechanical deformations on the thermal transport properties of isolated Mo_6S_6 NW was investigated by non-equilibrium molecular dynamics simulations with the first-principles-based ReaxFF forcefield. The low-frequency phonon thermal conductivity (κ_{lf}) of the Mo_6S_6 NW could be modulated mechanically from 42.3 to 191 W (m K)$^{-1}$ or from 27.2 to 64.1 W (m K)$^{-1}$ *via* tensile or torsional strains, respectively. Interestingly, the κ_{lf} of the Mo_6S_6 NW exhibits tensile/torsional strain-induced crossover as well as strain-induced negative Poisson's ratio. Under tension, the Mo_6S_6 NW shows κ_{lf} reduction tendency under tensile strains of <0.015 but κ_{lf} increases with increasing tensile strain. However, when subjected to twisting, the κ_{lf} is enhanced under torsional strain of <42.4° nm^{-1}, but is then reduced with further increase in torsional strain. Under small tensile/torsional deformations, there was a corresponding reduction/enlargement of the phonon group velocity, thereby reducing/enhancing κ accordingly. On the other hand, there was also a crossover in the values negative Poisson's ratio under tensile strain. This study provides important insights into the thermal conduction properties of the low-dimensional molybdenum chalcogenide structures, which are of importance toward the thermal management of the Mo_6S_6 NW-based devices and their thermoelectric applications.

Conflicts of interest

There are no conflicts to declare.

Acknowledgements

This work is financially supported by the National Natural Science Foundation of China (Grant No. 11772278, 12172314 and 11904300), the Jiangxi Provincial Outstanding Young Talents Program (Grant No. 20192BCBL23029), the Natural Science Foundation of Guangdong Province (Grant No. 2019A1515012183), the Fundamental Research Funds for the Central Universities (Xiamen University: Grant No. 20720210025). Y. Yu and Z. Xu from Information and Network Center of Xiamen University for the help with the high-performance computer.

References

1 H. J. Conley, B. Wang, J. I. Ziegler, R. F. Haglund, S. T. Pantelides and K. I. Bolotin, *Nano Lett.*, 2013, **13**, 3626–3630.
2 T.-X. Huang, X. Cong, S.-S. Wu, K.-Q. Lin, X. Yao, Y.-H. He, J.-B. Wu, Y.-F. Bao, S.-C. Huang, X. Wang, P.-H. Tan and B. Ren, *Nat. Commun.*, 2019, **10**, 5544.
3 I. Popov, T. Yang, S. Berber, G. Seifert and D. Tománek, *Phys. Rev. Lett.*, 2007, **99**, 085503.
4 Q.-l. Xiong, T. Kitamura and Z.-h. Li, *J. Appl. Phys.*, 2017, **122**, 135105.
5 X. Yin, Z. Ye, D. A. Chenet, Y. Ye, K. O'Brien, J. C. Hone and X. Zhang, *Science*, 2014, **344**, 488.

6 E. L. Ivchenko and B. Spivak, *Phys. Rev. B: Condens. Matter Mater. Phys.*, 2002, **66**, 155404.
7 H. Meng, S. Maruyama, R. Xiang and N. Yang, *Int. J. Heat Mass Transfer*, 2021, **180**, 121773.
8 D. B. Zhang, T. Dumitrica and G. Seifert, *Phys. Rev. Lett.*, 2010, **104**, 065502.
9 J. Kibsgaard, A. Tuxen, M. Levisen, E. Lægsgaard, S. Gemming, G. Seifert, J. V. Lauritsen and F. Besenbacher, *Nano Lett.*, 2008, **8**, 3928–3931.
10 I. Vilfan and D. Mihailovic, *Phys. Rev. B: Condens. Matter Mater. Phys.*, 2006, **74**, 235411.
11 I. Popov, S. Gemming, S. Okano, N. Ranjan and G. Seifert, *Nano Lett.*, 2008, **8**, 4093–4097.
12 P. Murugan, V. Kumar, Y. Kawazoe and N. Ota, *Nano Lett.*, 2007, **7**, 2214–2219.
13 S. Gemming, G. Seifert and I. Vilfan, *Phys. Status Solidi B*, 2006, **243**, 3320–3324.
14 Y. Zhou, Z. Fan, G. Qin, J.-Y. Yang, T. Ouyang and M. Hu, *ACS Omega*, 2018, **3**, 3278–3284.
15 K. Sääskilahti, J. Oksanen, S. Volz and J. Tulkki, *Phys. Rev. B: Condens. Matter Mater. Phys.*, 2015, **91**, 115426.
16 P. Koskinen, *Phys. Rev. Appl.*, 2016, **6**, 034014.
17 D. F. Souza, A. L. Rosa, P. Venezuela, J. E. Padilha, A. Fazzio and R. B. Pontes, *Phys. Rev. B*, 2019, **100**, 235416.
18 D. Çakır, E. Durgun, O. Gülseren and S. Ciraci, *Phys. Rev. B: Condens. Matter Mater. Phys.*, 2006, **74**, 235433.
19 X. Liu, T. Xu, X. Wu, Z. Zhang, J. Yu, H. Qiu, J.-H. Hong, C.-H. Jin, J.-X. Li, X.-R. Wang, L.-T. Sun and W. Guo, *Nat. Commun.*, 2013, **4**, 1776.
20 J. Lin, O. Cretu, W. Zhou, K. Suenaga, D. Prasai, K. I. Bolotin, N. T. Cuong, M. Otani, S. Okada, A. R. Lupini, J.-C. Idrobo, D. Caudel, A. Burger, N. J. Ghimire, J. Yan, D. G. Mandrus, S. J. Pennycook and S. T. Pantelides, *Nat. Nanotechnol.*, 2014, **9**, 436–442.
21 W. Yu, C. Liu, L. Qiu, P. Zhang, W. Ma, Y. Yue, H. Xie and L. S. Larkin, *Eng. Sci.*, 2018, **2**, 1–3.
22 C.-P. Feng, L.-B. Chen, G.-L. Tian, S.-S. Wan, L. Bai, R.-Y. Bao, Z.-Y. Liu, M.-B. Yang and W. Yang, *ACS Appl. Mater. Interfaces*, 2019, **11**, 18739–18745.
23 S. Berber, Y.-K. Kwon and D. Tománek, *Phys. Rev. Lett.*, 2000, **84**, 4613–4616.
24 M. Fujii, X. Zhang, H. Xie, H. Ago, K. Takahashi, T. Ikuta, H. Abe and T. Shimizu, *Phys. Rev. Lett.*, 2005, **95**, 065502.
25 B. Kumanek and D. Janas, *J. Mater. Sci.*, 2019, **54**, 7397–7427.
26 S. Plimpton, *J. Comput. Phys.*, 1995, **117**, 1–19.
27 Large-scale atomic/molecular massively parallel simulator, http://lammps.sandia.gov.
28 N. C. Osti, M. Naguib, A. Ostadhossein, Y. Xie, P. R. C. Kent, B. Dyatkin, G. Rother, W. T. Heller, A. C. T. van Duin, Y. Gogotsi and E. Mamontov, *ACS Appl. Mater. Interfaces*, 2016, **8**, 8859–8863.
29 A. Ostadhossein, E. D. Cubuk, G. A. Tritsaris, E. Kaxiras, S. Zhang and A. C. T. van Duin, *Phys. Chem. Chem. Phys.*, 2015, **17**, 3832–3840.
30 K. Yoon, A. Ostadhossein and A. C. T. van Duin, *Carbon*, 2016, **99**, 58–64.
31 M. M. Islam, A. Ostadhossein, O. Borodin, A. T. Yeates, W. W. Tipton, R. G. Hennig, N. Kumar and A. C. T. van Duin, *Phys. Chem. Chem. Phys.*, 2015, **17**, 3383–3393.
32 A. Ostadhossein, A. Rahnamoun, Y. Wang, P. Zhao, S. Zhang, V. H. Crespi and A. C. T. van Duin, *J. Phys. Chem. Lett.*, 2017, **8**, 631–640.
33 C. Lin, X. Chen and X. Zou, *ACS Appl. Mater. Interfaces*, 2019, **11**, 25547–25555.
34 H. Farahani, A. Rajabpour, M. Khanaki and A. Reyhani, *Comput. Mater. Sci.*, 2018, **142**, 1–6.
35 T. Liang, S. R. Phillpot and S. B. Sinnott, *Phys. Rev. B: Condens. Matter Mater. Phys.*, 2009, **79**, 245110.
36 J.-W. Jiang, *Nanotechnology*, 2015, **26**, 315706.
37 J. Kibsgaard, *PhD Thesis PhD*, Aarhus Universitetsforlag, 2008.
38 A. J. Gabourie, Z. Fan, T. Ala-Nissila and E. Pop, *Phys. Rev. B*, 2021, **103**, 205421.
39 H. Meng, D. Ma, X. Yu, L. Zhang, Z. Sun and N. Yang, *Int. J. Heat Mass Transfer*, 2019, **145**, 118719.
40 K. Xu, A. J. Gabourie, A. Hashemi, Z. Fan, N. Wei, A. B. Farimani, H.-P. Komsa, A. V. Krasheninnikov, E. Pop and T. Ala-Nissila, *Phys. Rev. B*, 2019, **99**, 054303.
41 S. Chen, A. Sood, E. Pop, K. E. Goodson and D. Donadio, *2D Mater.*, 2019, **6**, 025033.
42 J.-W. Jiang, H. S. Park and T. Rabczuk, *J. Appl. Phys.*, 2013, **114**, 064307.
43 Z. Xu and M. J. Buehler, *Nanotechnology*, 2009, **20**, 185701.
44 J.-W. Jiang, N. Yang, B.-S. Wang and T. Rabczuk, *Nano Lett.*, 2013, **13**, 1670–1674.
45 Q. Zhang, Z. Cui, Z. Wei, S. Y. Chang, L. Yang, Y. Zhao, Y. Yang, Z. Guan, Y. Jiang, J. Fowlkes, J. Yang, D. Xu, Y. Chen, T. T. Xu and D. Li, *Nano Lett.*, 2017, **17**, 3550–3555.
46 Q. Song, M. An, X. Chen, Z. Peng, J. Zang and N. Yang, *Nanoscale*, 2016, **8**, 14943–14949.
47 N. Yang, X. Ni, J.-W. Jiang and B. Li, *Appl. Phys. Lett.*, 2012, **100**, 093107.
48 D. Ma, A. Arora, S. Deng, G. Xie, J. Shiomi and N. Yang, *Mater. Today Phys.*, 2019, **8**, 56–61.
49 X. Wan, D. Ma, D. Pan, L. Yang and N. Yang, *Mater. Today Phys.*, 2021, **20**, 100445.
50 D. Ma, X. Wan and N. Yang, *Phys. Rev. B*, 2018, **98**, 245420.
51 B. L. Davis and M. I. Hussein, *Phys. Rev. Lett.*, 2014, **112**, 055505.
52 J. Shin, J. Sung, M. Kang, X. Xie, B. Lee, K. M. Lee, T. J. White, C. Leal, N. R. Sottos, P. V. Braun and D. G. Cahill, *Proc. Natl. Acad. Sci. U. S. A.*, 2019, **116**, 5973.
53 S. Deng, D. Ma, G. Zhang and N. Yang, *J. Mater. Chem. A*, 2021, **9**, 24472–24479.
54 L. Dong, Q. Xi, J. Zhou, X. Xu and B. Li, *Phys. Rev. Appl.*, 2020, **13**, 034019.
55 F. Hao, X. Liao, H. Xiao and X. Chen, *Nanotechnology*, 2016, **27**, 155703.

56 Z.-Y. Ong, Y. Cai, G. Zhang and Y.-W. Zhang, *J. Phys. Chem. C*, 2014, **118**, 25272–25277.
57 R. Tu, Q. Liao, L. Zeng, Z. Liu and W. Liu, *Appl. Phys. Lett.*, 2017, **110**, 101905.
58 H. Shen, *Mol. Phys.*, 2014, **112**, 2614–2620.
59 H. Xie, T. Ouyang, É. Germaneau, G. Qin, M. Hu and H. Bao, *Phys. Rev. B*, 2016, **93**, 075404.
60 M. Khalkhali and F. Khoeini, *J. Phys. Chem. Solids*, 2018, **112**, 216–221.
61 C. Ren, W. Zhang, Z. Xu, Z. Zhu and P. Huai, *J. Phys. Chem. C*, 2010, **114**, 5786–5791.
62 G. Lei and H. Liu, *J. Mater. Sci.*, 2018, **53**, 1310–1317.
63 J.-S. Wang and B. Li, *Phys. Rev. Lett.*, 2004, **92**, 074302.
64 N. Yang, G. Zhang and B. Li, *Nano Today*, 2010, **5**, 85–90.
65 C. Deng, Y. Huang, M. An and N. Yang, *Mater. Today Phys.*, 2021, **16**, 100305.
66 Y. Zhou, X. Zhang and M. Hu, *Nano Lett.*, 2017, **17**, 1269–1276.
67 C. Zhang, D. Ma, M. Shang, X. Wan, J.-T. Lü, Z. Guo, B. Li and N. Yang, *Mater. Today Phys.*, 2022, 100605, DOI: 10.1016/j.mtphys.2022.100605.
68 M. Raeisi, S. Ahmadi and A. Rajabpour, *Nanoscale*, 2019, **11**, 21799–21810.
69 S. Deng, J. Yuan, Y. Lin, X. Yu, D. Ma, Y. Huang, R. Ji, G. Zhang and N. Yang, *Nano Energy*, 2021, **82**, 105749.
70 J. A. Thomas, J. E. Turney, R. M. Iutzi, C. H. Amon and A. J. H. McGaughey, *Phys. Rev. B: Condens. Matter Mater. Phys*, 2010, **81**, 081411.
71 Z. Ding, Q.-X. Pei, J.-W. Jiang and Y.-W. Zhang, *J. Phys. Chem. C*, 2015, **119**, 16358–16365.
72 H. Liu, G. Qin, Y. Lin and M. Hu, *Nano Lett.*, 2016, **16**, 3831–3842.
73 A. Taheri, C. Da Silva and C. H. Amon, *Phys. Chem. Chem. Phys.*, 2018, **20**, 27611–27620.
74 H. Gu and H. Wang, *Comput. Mater. Sci.*, 2018, **144**, 133–138.
75 S. Li, X. Yu, H. Bao and N. Yang, *J. Phys. Chem. C*, 2018, **122**, 13140–13147.
76 J. Liu and R. Yang, *Phys. Rev. B: Condens. Matter Mater. Phys.*, 2010, **81**, 174122.
77 B. Ding, X. Li, W. Zhou, G. Zhang and H. Gao, Anomalous strain effect on the thermal conductivity of low-buckled two-dimensional silicene, *Natl. Sci. Rev.*, 2020, **8**(9), DOI: 10.1093/nsr/nwaa220.
78 B. Mortazavi, M.-Q. Le, T. Rabczuk and L. F. C. Pereira, *Phys. E*, 2017, **93**, 202–207.
79 Y.-Y. Zhang, Q.-X. Pei, J.-W. Jiang, N. Wei and Y.-W. Zhang, *Nanoscale*, 2016, **8**, 483–491.
80 H. Du, G. Li, J. Chen, Z. Lv, Y. Chen and S. Liu, *Phys. Chem. Chem. Phys.*, 2020, **22**, 20107–20113.
81 S. Liu, H. Du, G. Li, L. Li, X. Shi and B. Liu, *Phys. Chem. Chem. Phys.*, 2018, **20**, 20615–20621.
82 R. Qin, J. Zheng and W. Zhu, *Nanoscale*, 2017, **9**, 128–133.
83 S. Safaei, R. Tavakoli and M. Jafary-Zadeh, *Comput. Mater. Sci.*, 2018, **153**, 258–267.
84 B. Wang, Q. Wu, Y. Zhang, L. Ma and J. Wang, *ACS Appl. Mater. Interfaces*, 2019, **11**, 33231–33237.
85 Y. Wang, F. Li, Y. Li and Z. Chen, *Nat. Commun.*, 2016, **7**, 11488.
86 C. Zhang, T. He, S. K. Matta, T. Liao, L. Kou, Z. Chen and A. Du, *J. Phys. Chem. Lett.*, 2019, **10**, 2567–2573.
87 Q. Zhang, Y. Feng, X. Chen, W. Zhang, X. Wu, L. Wu and Y. Wang, *Comput. Mater. Sci.*, 2019, **168**, 87–95.
88 G. F. Xie, Z. F. Ju, K. K. Zhou, X. L. Wei, Z. X. Guo, Y. Q. Cai and G. Zhang, Ultra-low thermal conductivity of two-dimensional phononic crystals in the incoherent regime, *npj Comput. Mater*, 2018, **4**(21), DOI: 10.1038/s41524-018-0076-9.
89 J. Y. Wu, J. Y. He and Z. L. Zhang, *Comput. Mater. Sci.*, 2013, **80**, 15–26.
90 X. L. Zhu, H. Y. Yang, W. X. Zhou, B. T. Wang, N. Xu and G. F. Xie, KAgX (X = S, Se): High-Performance Layered Thermoelectric Materials for Medium-Temperature Applications, *ACS Appl. Mater. Interfaces*, 2020, **12**(32), 36102–36109.
91 C. Zhang, D. K. Ma, M. Y. Shang, X. Wan, J. T. Lü, Z. L. Guo, B. W. Li and N. Yang, Graded thermal conductivity in 2D and 3D homogeneous hotspot systems, *Mater. Today Phys.*, 2022, **22**, 100605.

Supporting Information

Efficient mechanical modulation of the phonon thermal conductivity of Mo_6S_6 nanowires

Ke Xu,[1, #] Shichen Deng,[2, #] Ting Liang,[3] Xuezheng Cao,[1] Meng Han,[3] Xiaoliang Zeng,[3] Zhisen Zhang,[1] Nuo Yang,[2, a)] and Jianyang Wu[1, 4, b)]

[1]Department of Physics, Research Institute for Biomimetics and Soft Matter, Jiujiang Research Institute and Fujian Provincial Key Laboratory for Soft Functional Materials Research, Xiamen University, Xiamen 361005, PR China

[2]State Key Laboratory of Coal Combustion, and School of Energy and Power Engineering, Huazhong University of Science and Technology (HUST), Wuhan, 430074 PR China

[3]Shenzhen Institute of Advanced Electronic Materials, Shenzhen Institutes of Advanced Technology, Chinese Academy of Sciences, Shenzhen 518055, PR China

[4]NTNU Nanomechanical Lab, Norwegian University of Science and Technology (NTNU), Trondheim 7491, Norway

[#] These authors contributed equally to this work.
[a)] Electronic mail: nuo@hust.edu.cn (N. Y.)
[b)] Electronic mail: jianyang@xmu.edu.cn (J. W.)

1. Molecular Models of Deformed Mo_6S_6 Nanowire

Table S1 lists the detailed information of both stretched and twisted Mo_6S_6 nanowires. All the investigated atomic models of Mo_6S_6 nanowires are composed of identical number of atoms (6000). However, as a result of axial elongation and twisting deformation, they show different lattice constants in axial direction. Figure S1 shows the detailed structural information of Mo_6S_6 nanowires subjected to axial tension and torsional strain.

Table S1 Structural information of mechanically-deformed Mo_6S_6 nanowires

Stretched Nanowires					No. 6000			
Tensile Strain (m/m)	0.0	0.005	0.01	0.015	0.02	0.025	0.03	0.04
Axial Length $\mathbf{C_1}$ (Å)	4.60	4.63	4.65	4.67	4.69	4.72	4.74	4.79
Twisted Nanowires					No. 6000			
Torsional Strain (°/nm)	0.0	10.5	21.0	31.7	42.4	53.3	64.2	75.2
Axial Length $\mathbf{C_1}$ (Å)	4.60	4.58	4.57	4.55	4.53	4.51	4.49	4.47

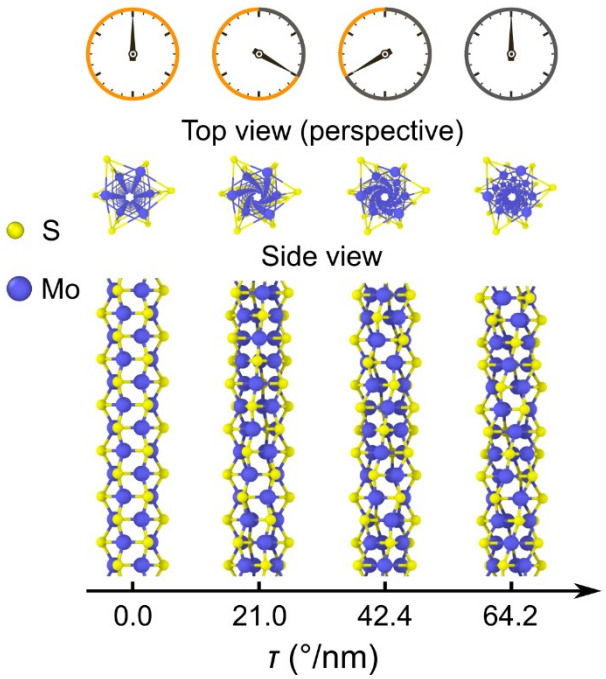

Figure S1 Schematic of Mo_6S_6 nanowire subjected to four different torsional strains (τ) that are 0.0, 21.0, 42.4 and 64.2°/nm, respectively. For top schematic, the clockwise rotation is used to indicate the

twisting angles of Mo_6S_6 nanowire. For bottom-viewed atomic models, the Mo and S atoms in Mo_6S_6 nanowire are yellow- and blue-colored for clarification.

2. Methodology

2.1 Settings of NEMD simulations

The detailed setting parameters of all NEMD simulations are listed in Table S2. ReaxFF potential is a powerful tool to study a wide range of systems[1-4]. On the other hand, the popular forcefields of Mo-S type REBO[5] and SW[6] are tested, While, both Mo-S type REBO[5] and SW forcefields are not able to stabilize Mo_6S_6 nanowire. A small timestep of 0.2 fs is adopted to perform the NEMD. For Mo-S systems, ReaxFF forcefield was also adopted to study the thermal[7, 8] and mechanical properties[9, 10]. The simulation procedure is summarized as follows. After minimization, the NPT ensemble is used to relax the Mo_6S_6 nanowire structure for 1 ns. Then, except for the thermostat regions, the rest of the system is simulated by NVE ensemble for 8 ns to reach the steady state. Finally, a longer simulation using NVE ensemble is performed for 2 ns to record and average the temperature and heat flux. Here, we use a more efficient NEMD method with fixed boundaries, as shown in Figure S2b.

Table S2. NEMD simulation details

Method	Non-Equilibrium molecular dynamics		
Parameters			
Potential	ReaxFF	**Time step**	0.2 fs
Thermostat	Langevin	**Temperature difference**	30 K
Simulation process			
Ensemble	**Setting**		**Purpose**
NVT	Boundary condition	x, y, z: p, p, f	Relax structure
	Runtime	1 ns	
NVE	Boundary condition	x, y, z: p, p, f	Reach steady state
	Runtime	8 ns	
NVE	Boundary condition	x, y, z: p, p, f	Reach information
	Runtime	2 ns	
Recorded physical quantity			

Temperature	$\langle E \rangle = \sum_{i=1}^{N} \frac{1}{2} m^i v_i^2 = \frac{3}{2} N k_B T$
Heat flux	$J = \frac{\Delta E_{in} + \Delta E_{out}}{2\Delta t}$
Thermal conductivity	$\kappa = -\frac{J}{A\nabla T} = -\frac{JL}{A\Delta T}$

2.2 NEMD method

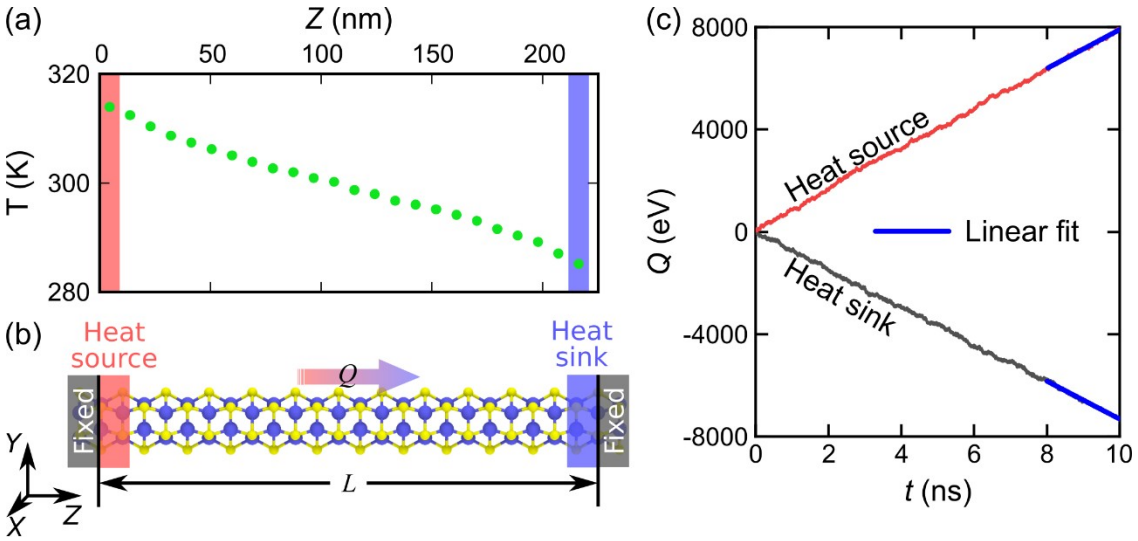

Figure S2 (a) Steady-state temperature profile in the Mo_6S_6 system. (b) The axial direction of the tube is the *z* direction, and the heat flow (Q) transfer is imposed in this direction. (c) The energy of the source and sink thermostat as a function of the time in steady state.

3 The phonon thermal conductivity

3.1 Phonon transmission spectra and Accumulated thermal conductivity

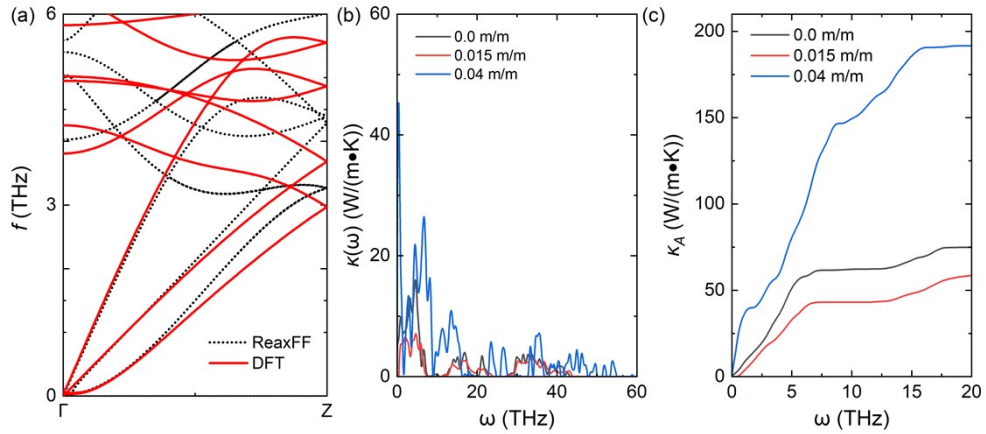

Figure S3. (a) Phonon dispersion predicted by ReaxFF-based MD calculations and DFT calculations ($\omega<\omega^{A}_{max}$, ω^{A}_{max}=6 THz). (b) Phonon transmission spectra ($\kappa(\omega)$) of Mo_6S_6 nanowire with frequency (ω) range at 0-60 THz. (c) Accumulated thermal conductivity (κ_A) of Mo_6S_6 nanowire with frequency (ω) range at 0-20 THz.

Here, the spectral thermal conductivity of Mo_6S_6 NW is calculated from the transmission coefficient, as shown in Figure S3(a). As is indicated, the thermal conductivity of Mo_6S_6 NW subjected to zero strain is largely contributed by the low-frequency region. Such case is also identified as Mo_6S_6 NW is stretched and twisted, as shown in the Figure S3(b). Therefore, the dependence of the thermal conductivity on mechanical strains is dictated by low-frequency contributions.

To verify the accuracy of our ReaxFF-based MD results, the phonon spectrum is also predicted by density functional theory (DFT) calculations, as shown in the Figure S3(c). The black dashed lines are the phonon dispersion relation curves of Mo_6S_6 NW at zero strain obtained from a lattice dynamic program Phonopy[11]. The phonon dispersion with DFT calculations was extracted from VASP[12] (Vienna Ab initio Simulation Package), in which the PBE was used for the exchange-correlation

functional, and self-consistent calculation was performed with a cutoff energy of 600 eV and a force convergence criterion of 10^{-7} eV/Å. By comparison, it is found that phonon spectrogram of Mo_6S_6 NW in the low-frequency region predicted by ReaxFF-based MD calculations are in good agreement with that by DFT calculations. Given that the thermal conductivity of Mo_6S_6 NW by ReaxFF-based MD simulations is largely contributed by the low-frequency region. Therefore, the thermal conductivity of Mo_6S_6 NW by ReaxFF-based MD calculations is reliable.

3.2 Phonon thermal conductivity and *v*DOS of full frequency.

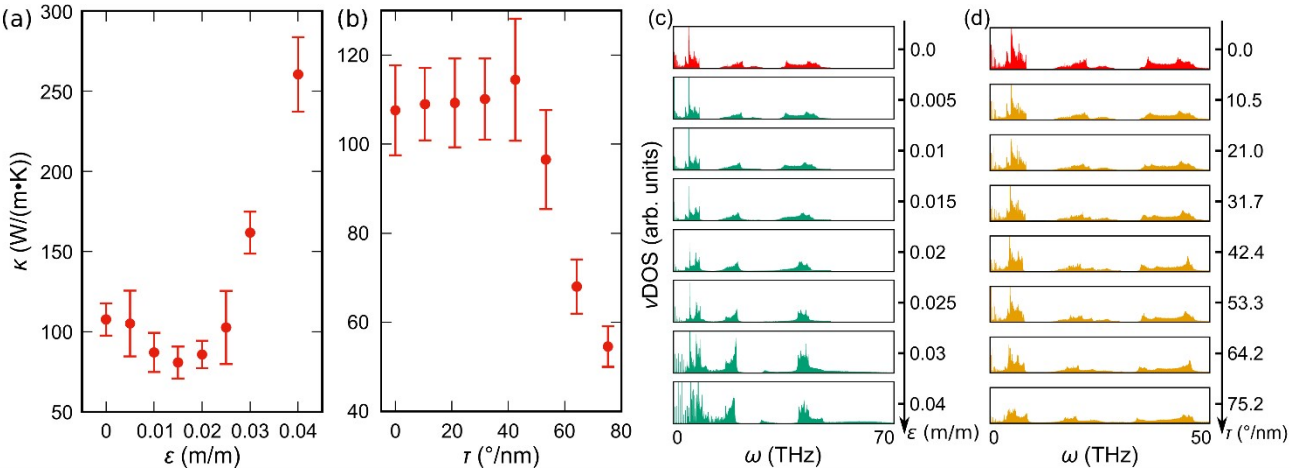

Figure S4 (a) and (b) Variations in the phonon thermal conductivity (*v*DOS) of Mo_6S_6 nanowire with tensile (ε) and torsional (τ) strains, respectively. (c) and (d) *v*DOS of isolated Mo_6S_6 nanowire subjected to different tensile and torsional strains.

As shown in the Figures S3(c-d), the upper-bound frequency is increased, for example, it reaches about 65 THz at axial tension strain of 0.04. Such strain-induced transition change in the vDOS spectra explains the crossover of phonon thermal conductivity in Mo_6S_6 NW.

3.3 Size effect and three-phonon scattering

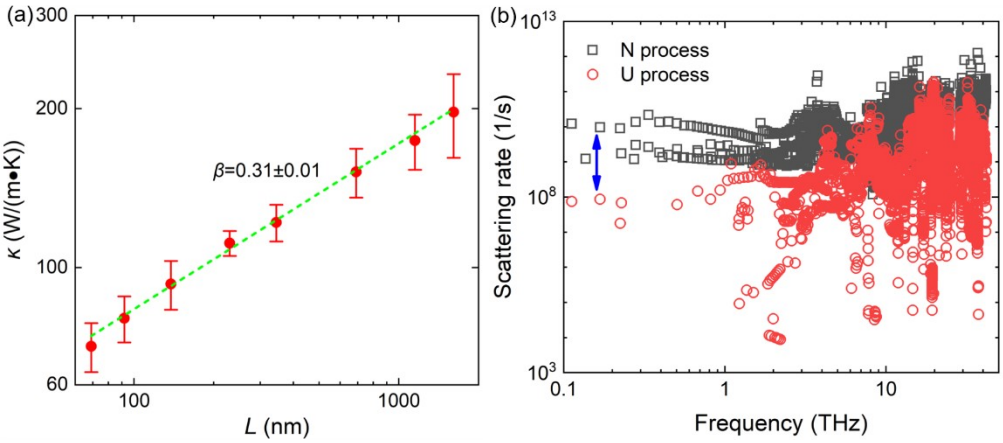

Figure S5. (a) Thermal conductivity (κ) for Mo_6S_6 nanowire at 300 K with different lengths (L) from the NEMD simulations. (b) Three-phonon scattering rates in Mo_6S_6 nanowires subjected to zero strain as a function of phonon frequency, including Normal and Umklapp processes.

It is well known that there is size effect on the thermal conductivity of low-dimensional materials. As shown in the Figure S5a, the size effect of thermal conductivity of Mo_6S_6 NW is also examined. Figure R4 shows the variation in the thermal conductivity of Mo_6S_6 NW with axial length. It is revealed that the thermal conductivity of Mo_6S_6 NW follows $\kappa \propto L^{\beta}$, and here $\beta = 0.31$. This suggests that the thermal conductivity of Mo_6S_6 NW follows one-dimensional (1D) nonlinear lattice model. Our results are in good agreement with previous predictions of 1D nanostructure, namely, the thermal conductivity of 1D materials is length dependent[13, 14]. In our study, Mo_6S_6 NW with finite axial length of 200 nm is generated to reveal the role of tension and torsion strains on the thermal conductivity.

As shown in Figure S5b, we calculated the three-phonon scattering rates of the Mo_6S_6 NW. The three-phonon scattering rates is calculated by PHONO3PY[15] and includes the Normal process and Umklapp process. The third-order interatomic force constants, with an atomic displacement of 0.03 Å,

is calculated from the finite difference method. As is indicated, the normal (N) process is around two orders of magnitudes stronger than the Umklapp (U) process in low-frequency range (< 1 THz).

3.4 Phonon dispersion relationship

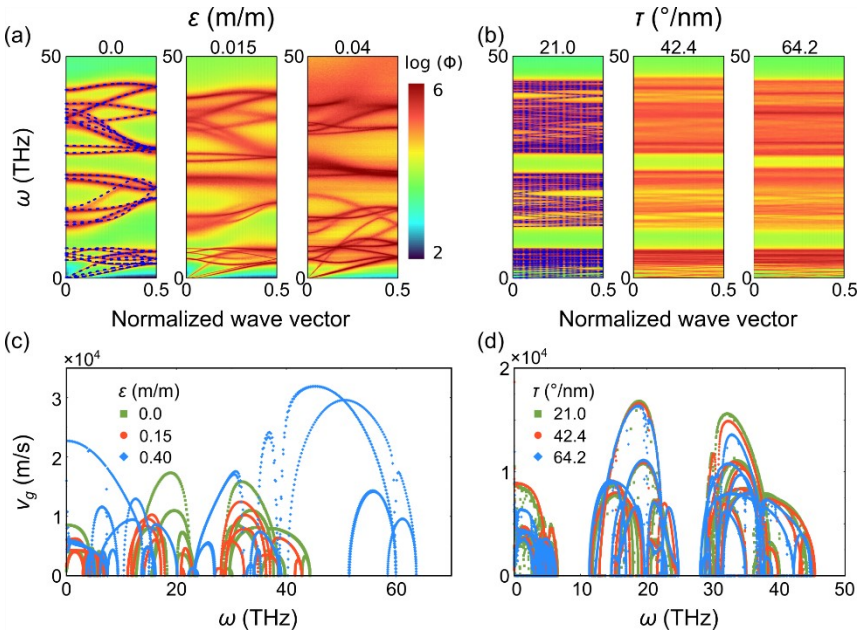

Figure S6 (a) and (b) Phonon dispersion relationship of isolated Mo_6S_6 nanowire subjected to three critical tensile (ε) and torsional (τ) strains, respectively. (c) and (d) Phonon group velocity (v_g) as a function of frequency (ω) for isolated Mo_6S_6 nanowire under three critical tensile (ε) and torsional (τ) strains, respectively.

The blue dashed lines are the phonon dispersion relation curves of Mo_6S_6 NW at zero strain obtained from a lattice dynamic program Phononpy[11]. As shown in the Figure S4, the highest frequency is enlarged to about 65 THz, but at high frequency region, the SED curves are not able to distinguish, indicating severe phonon scattering. The high frequency phonons cover a wide frequency range, and the group velocity is tripled, thereby resulting in increase in the phonon thermal conductivity.

4. Bond length distribution

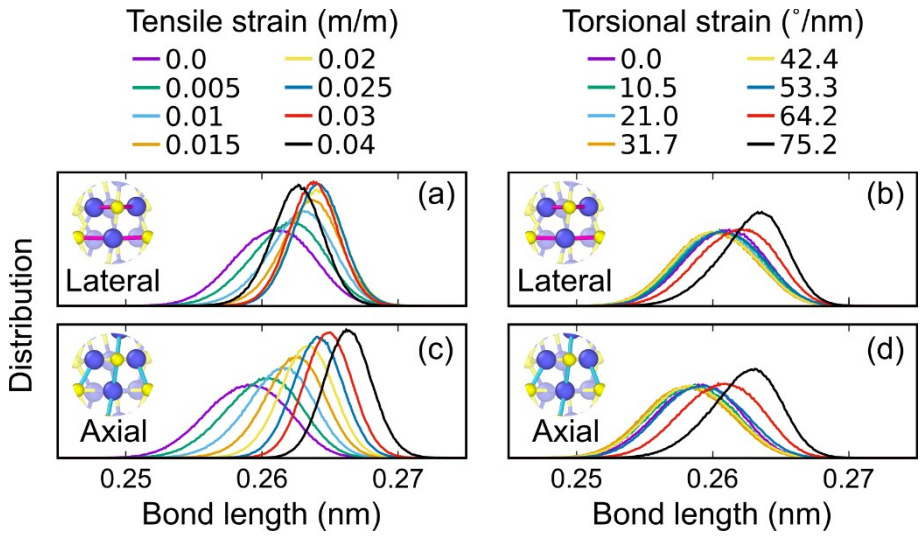

Figure S7 (a) and (c) Distribution of bond length of unique Mo-S bond that makes 0° and 90° angles to the axial direction of wire as the Mo_6S_6 nanowire is subjected to different tension strains (ε), respectively. (a) and (c) Distribution of bond length of unique Mo-S bond that makes 0° and 90° angles to the axial direction of wire as the Mo_6S_6 nanowire is subjected to different torsional strains (τ) respectively.

References

1. N. C. Osti, M. Naguib, A. Ostadhossein, Y. Xie, P. R. C. Kent, B. Dyatkin, G. Rother, W. T. Heller, A. C. T. van Duin, Y. Gogotsi and E. Mamontov, *ACS Appl. Mater. Interfaces*, 2016, **8**, 8859-8863.
2. A. Ostadhossein, E. D. Cubuk, G. A. Tritsaris, E. Kaxiras, S. Zhang and A. C. T. van Duin, *Phys. Chem. Chem. Phys.*, 2015, **17**, 3832-3840.
3. K. Yoon, A. Ostadhossein and A. C. T. van Duin, *Carbon*, 2016, **99**, 58-64.
4. M. M. Islam, A. Ostadhossein, O. Borodin, A. T. Yeates, W. W. Tipton, R. G. Hennig, N. Kumar and A. C. T. van Duin, *Phys. Chem. Chem. Phys.*, 2015, **17**, 3383-3393.
5. T. Liang, S. R. Phillpot and S. B. Sinnott, *Phys. Rev. B*, 2009, **79**, 245110.
6. J.-W. Jiang, *Nanotechnology*, 2015, **26**, 315706.
7. B. Mortazavi, R. Quey, A. Ostadhossein, A. Villani, N. Moulin, A. C. T. van Duin and T. Rabczuk, *Applied Materials Today*, 2017, **7**, 67-76.
8. H. Farahani, A. Rajabpour, M. Khanaki and A. Reyhani, *Comput. Mater. Sci.*, 2018, **142**, 1-6.
9. B. Mortazavi, A. Ostadhossein, T. Rabczuk and A. C. T. van Duin, *Phys. Chem. Chem. Phys.*, 2016, **18**, 23695-23701.
10. A. Ostadhossein, A. Rahnamoun, Y. Wang, P. Zhao, S. Zhang, V. H. Crespi and A. C. T. van Duin, *J. Phys. Chem. Lett.*, 2017, **8**, 631-640.
11. A. Togo and I. Tanaka, *Scripta Mater.*, 2015, **108**, 1-5.

12. G. Kresse and J. Furthmüller, *Phys. Rev. B*, 1996, **54**, 11169-11186.
13. J.-S. Wang and B. Li, *Phys. Rev. Lett.*, 2004, **92**, 074302.
14. N. Yang, G. Zhang and B. Li, *Nano Today*, 2010, **5**, 85-90.
15. A. Togo, L. Chaput and I. Tanaka, *Phys. Rev. B*, 2015, **91**, 094306.